Simulation and visualization of attosecond stimulated x-ray Raman spectroscopy signals in *trans*-N-methylacetamide at the nitrogen and oxygen K-edges

Daniel Healion, Haitao Wang, and Shaul Mukamel[a)]
Department of Chemistry, University of California, Irvine, California 92697-2025, USA

(Received 2 December 2010; accepted 1 February 2011; published online 22 March 2011)

The stimulated Raman component of the pump-probe spectrum of *trans*-N-methylacetamide obtained in response to two soft x-ray pulses is calculated by treating the core excitations at the Hartree–Fock static-exchange level. The signal reveals the dynamics of valence-electron wave packets prepared and detected in the vicinity of a selected atom (either nitrogen or oxygen). The evolving electronic charge density as well as electronic coherence of the doorway and the window created by the two pulses are visualized using a time-dependent basis set of natural orbitals, which reveals that the wave packets consist of several entangled valence particle–hole pairs. © *2011 American Institute of Physics*. [doi:10.1063/1.3557057]

I. INTRODUCTION

The development of bright attosecond soft and hard x-ray pulses, both x-ray lasers and table top high harmonic generation sources, has triggered considerable interest in all-x-ray nonlinear spectroscopy measurements.[1–10] Resonant interaction with x-ray pulses causes multiple excitation and de-excitation events involving core electrons, which are accompanied by valence electronic excitations. X-ray techniques offer a high temporal resolution and a bird-eye view of many-body valence electronic excitations covered by the broad bandwidth (18 eV for a 100 as pulse). Resonant optical spectroscopy, in contrast, looks at one electronic state at a time and often has strict selection rules that limit the number and type of accessible states.

In a recently proposed pump-probe experiment,[11,12] the interaction with an attosecond x-ray pump tuned resonantly to a specific core–hole transition launches an electronic wave packet via a Raman process which spans valence excitations as permitted by the finite pump bandwidth, which is then detected by a delayed x-ray probe. The dependence of the probe absorption on the delay time provides information on the evolving wave packet. Since core shells are highly localized, the wave packet is initially centered at the atom whose core shell is in resonance with the pump frequency. Similarly, the probe absorption reflects the unoccupied states in the vicinity of the core shell in resonance with the probe frequency. By tuning the pump and probe frequencies to different core transitions, one can select where the wave packet is created and where it is probed, thus studying the underlying electron motions with high temporal and spatial resolution.

In our earlier study,[12] the core-excited states were calculated by the valence-excited states of the equivalent-core (or, Z+1) molecule. Valence-excited states were represented by determinants made of the ground-state Hartree–Fock/density functional Kohn–Sham orbitals of the original and equivalent-core molecules. This equivalent-core approximation (ECA) (Ref. 13) relies on the fact that the core and valence electron energies are well separated, and thus weakly correlated. The effect of the created core-hole on the valence electrons is then reduced to that of a static Coulomb potential of a unit positive charge localized on the resonant core. This is a crude approximation to the core-excited electronic structure, and to the orbital relaxation effects upon electronic excitations from core orbitals.[14] In this paper, we calculate the stimulated x-ray Raman spectroscopy (SXRS) signal of N-methylacetamide (NMA), a small organic molecule used as a convenient model system for the peptide bond[15–17] forming the backbones of proteins, using a higher level description of core excitations, the static-exchange (STEX) approximation. STEX, developed by Ågren *et al.*,[18–21] offers a much improved description of orbital relaxation effects and of the virtual orbitals to which the core electrons are excited.[22]

Several all-x-ray four-wave mixing techniques were recently proposed by Schweigert and Mukamel.[6,12,23] The pump-probe technique described here is easier, since it only requires two pulses, and the signal is independent of their phases so that phase control is not required. The pulse intensity should be sufficiently high in order for the stimulated emission to compete with Auger process. Recent experiments[24,25] have shown that hollow atoms can be created by intense x-ray pulses. In future, sources of similar intensity tuned to the resonant core transitions of these atoms will be available. Ultrafast electronic dynamics following ionization for a similar system, the small amino acid glycine, were calculated in Ref. 26.

In a typical time-resolved pump-probe experiment which employs visible pulses, a short pump impulsively prepares a vibrational wave packet on an electronically excited potential energy surface (PES). Each discrete electronic eigenstate is represented as a sheet embedded in a high-dimensional space of nuclear coordinates. In core-excitation spectroscopy, this energy picture is extended to clumps of sheets with

a)Electronic mail: smukamel@uci.edu.

different core occupations, separated in energy by 100–1000 eV. Attosecond pulses are short enough to impulsively excite wave packets over nuclear *and* valence excited states. The Born–Oppenheimer factorization allows the nuclear and electronic coordinates to be separated except for specific regions, conical intersections, or seams in which adjacent PESs cross. These surface crossings can give rise to strong couplings between the electronic and nuclear degrees of freedom, and the Born–Oppenheimer approximation breaks down.[27,28] Here we solely focus on the electronic degrees of freedom, ignoring the fast electron-nuclear dynamics. A single ground state minimized geometry is held fixed during the experiment. The decay of valence excited states induced by these nuclear motions are also neglected.

The SXRS electronic signal is expressed using closed-time-path loop diagrams[29,30] in Sec. II. The necessary correlation functions are expanded in many-electron states. The stimulated Raman signal is recast in the doorway-window representation,[29,31,32] as the overlap of a doorway many-electron wave packet created by the pump and a window wave packet created by the probe. This representation provides an intuitive picture of the measurement by dividing the process into three stages: the wave packet creation, propagation, and detection. In Sec. III, the Raman signal is recast and visualized in terms of reduced particle–hole pairs in the natural orbital representation.

In Sec. IV, we study orbital relaxation effects following core electronic excitations by comparing the N and O K-edge x-ray absorption near-edge structure (XANES) at the ECA and STEX levels. In Sec. V, we present simulations of the N and O K-edge stimulated Raman signals for the N1*s* pump/N1*s* probe, N1*s* pump/O1*s* probe, O1*s* pump/N1*s* probe, and O1*s* pump/O1*s* probe pulse configurations. The particle–hole pairs that dominate the signal are described using a time-dependent basis set of natural orbital,[33] and their snapshots are interpreted in terms of a real space movie of the electron and hole dynamics. This picture is not limited to the time-resolved charge density as in electron diffraction, but carries phase information (electron coherence) as well. Conclusions are given in Sec. VI.

II. CLOSED-TIME-PATH LOOP DIAGRAMS FOR STIMULATED X-RAY RAMAN SIGNALS

The total Hamiltonian of a molecule interacting with x-ray fields which is partitioned as

$$H_{\text{total}} = H_{\text{mol}} + H_{\text{int}}. \tag{1}$$

In the molecular Hamiltonian

$$H_{\text{mol}} = \sum_i h_{ii} c_i^\dagger c_i + \frac{1}{2} \sum_{ijkl} \langle ij|kl\rangle c_i^\dagger c_j^\dagger c_l c_k, \tag{2}$$

the first term stands for the one-electron part containing the kinetic energy and the nuclear-electron attraction, while the second term is the electron–electron repulsion. Here, $c^\dagger(c)$ are Fermi creation (annihilation) operators.

The matter-field interaction in the rotating wave approximation is

$$H_{\text{int}} = \sum_n \left[E(t) V_n^\dagger + E^*(t) V_n \right], \tag{3}$$

where

$$V_n^\dagger = \sum_k \mu_{kn} c_k^\dagger c_n, \quad V_n = \sum_k \mu_{nk} c_k c_n^\dagger \tag{4}$$

are the creation and annihilation operators for core electronic excitations. Here, μ_{kn} is the dipole matrix element between the nth core orbital and the kth valence orbital, and $E(t)$ is the positive frequency part of the x-ray field. We shall consider pulses with frequencies tuned to the resonant soft x-ray regime, where the dipole approximation holds for core-excitations of low-Z atoms. The core orbital size may be larger than the wavelength of the exciting light for nonlinear hard x-ray experiments which involve photoionization of the core electron. This will require quadrupolar or higher multipole corrections to the matter-field interaction.

We subject the system to two attosecond x-ray pulses separated by a delay time τ

$$\begin{aligned} E(t) &= E_1(t) e^{i\boldsymbol{k}_1 \boldsymbol{r}} + E_2(t-\tau) e^{i\boldsymbol{k}_2 \boldsymbol{r}} \\ E_j(t) &= \mathcal{E}_j(t) e^{-i\omega_j t} \end{aligned} \tag{5}$$

where $\mathcal{E}_1(t)$, $\boldsymbol{k}_1$, and ω_1 are, respectively, the complex envelope, the wave vector, and the carrier frequency of the pump and $\mathcal{E}_2(t)$, $\boldsymbol{k}_2$, ω_2 are those of the probe.

The pump-probe signal, defined as the difference in the absorption of the probe, with and without the pump, generally has three contributions known as excited state stimulated emission (ESE), excited-state absorption (ESA), and ground-state bleaching (GSB).[6] In the ESE and ESA, the molecule is prepared by the pump in the core-excited states, whose lifetime ($\tau_c \sim 5-10$ fs for first-row atoms) is much shorter than that of valence-excited states (>1 ps). For delay times $\tau > \tau_c$, these contributions vanish and the signal is dominated by the GSB, which is a Raman-type SXRS contribution. The present study will focus on this regime. Following two interactions with the pump, a valence electronic wave packet (with no core-hole) is created, which spans the valence electronic states covered by the pump pulse bandwidth. Figure 1 depicts the level diagram for the SXRS

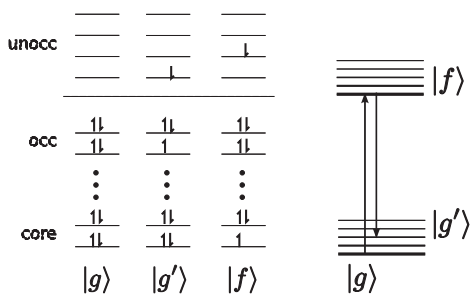

FIG. 1. The level scheme used in the present simulations. $|g\rangle$ is the ground state of the molecule and $|g'\rangle$ are the valence-excited states (with no core-hole). $|f\rangle$ are the valence-excited state manifolds with one core-hole localized on the nitrogen or oxygen atom selected by the pump or the probe.

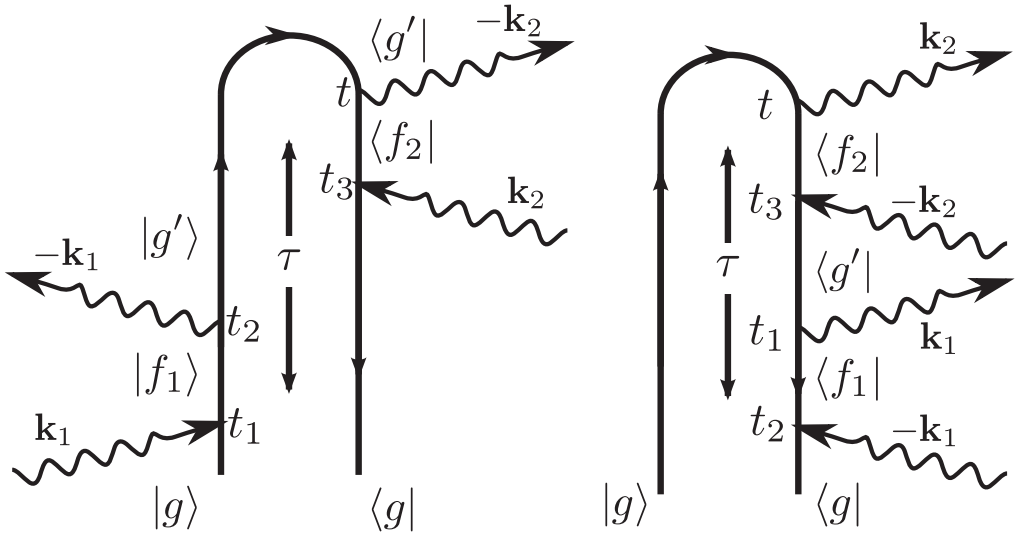

FIG. 2. The two closed-time-path loop diagrams that contribute to the stimulated Raman signal. (For rules see Refs. 6, 12, and 29.) The levels $|g\rangle$, $|g'\rangle$ and $|f\rangle$ are defined in Fig. 1.

experiment. $|g\rangle$ is the ground state of the molecule. $|g'\rangle$ are valence-excited states with no core-hole, $|f_1\rangle(|f_2\rangle)$ are core-excited states where an electron from core orbitals localized the atom resonant with pulse 1(2) is promoted to the valence orbital space. The signal can be interpreted in terms of the evolving valence electronic wave packet created upon core electronic excitation by using closed-time-path loop diagrams for the wave function shown in Fig. 2. This is more compact representation than the density matrix representation for the Liouville pathways.[12]

These diagrams give the following correlation function expression for the stimulated Raman signal:

$$S_{\mathrm{SXRS}}(\tau)=2\mathrm{Re}\int_{-\infty}^{\infty}dt\int_{-\infty}^{t}dt_3E_2(t-\tau)E_2^*(t_3-\tau)E_1^*(t_2)E_1(t_1)\times\Big[\int_{-\infty}^{\infty}dt_2\int_{-\infty}^{t_2}dt_1\big\langle V(t_3)V^\dagger(t)V(t_2)V^\dagger(t_1)\big\rangle+\int_{-\infty}^{\infty}dt_1\int_{-\infty}^{t_1}dt_2\big\langle V(t_2)V^\dagger(t_1)V(t_3)V^\dagger(t)\big\rangle\Big]. \tag{6}$$

All operators are in the interaction picture $V(t)=\exp(iH_{\mathrm{mol}}t)V\exp(-iH_{\mathrm{mol}}t)$. The dipole correlation functions can be expanded in the many-electron molecular states,

$$\big\langle V(\tau_4)V^\dagger(\tau_3)V(\tau_2)V^\dagger(\tau_1)\big\rangle=\sum_{g',f_1,f_2}V_{gf_2}V^\dagger_{f_2g'}V_{g'f_1}V^\dagger_{f_1g}\times\exp[-i\omega_{f_2g}\tau_4-i\omega_{g'f_2}\tau_3-i\omega_{f_1g}\tau_2-i\omega_{gf_1}\tau_1] \tag{7}$$

Substituting Eq. (7) in Eq. (6), we obtain

$$S_{\mathrm{SXRS}}(\tau)=2\mathrm{Re}\sum_{g'\neq g}\sum_{f_1,f_2}V_{gf_2}V_{f_2g'}V_{g'f_1}V_{f_1g}e^{-i\omega_{g'g}\tau-\Gamma_{g'}\tau}\times\int\frac{d\omega_2}{2\pi}E_2^*(\omega_2)E_2(\omega_2-\omega_{g'g})\times\mathrm{Im}\frac{1}{\omega_2-\omega_{g'g}-\omega_{f_2g}-i\Gamma_{f_2}}\times\int\frac{d\omega_1}{2\pi}E_1^*(\omega_1)E_1(\omega_1-\omega_{g'g})\times\frac{1}{\omega_1-\omega_{g'g}-\omega_{f_1g}+i\Gamma_{f_1}}, \tag{8}$$

where $\omega_{g'g}=\epsilon_{g'}-\epsilon_g$ is the transition frequency between valence-excited states and the ground state. Γ_i is the decay rate (inverse lifetime) of the state i, which was added here phenomenologically,

$$E_j(\omega)=\frac{1}{2\pi}\int e^{-i\omega t}E_j(t)\mathrm{d}t, \tag{9}$$

are the jth pulse envelop in the frequency domain. Hereafter, we shall assume Gaussian envelopes with bandwidth σ_j,

$$\mathcal{E}_j(t)=e^{-t^2\sigma_j^2/2}, \tag{10}$$

$$E_j(\omega)=\frac{1}{\sqrt{2\pi}\cdot\sigma_j}\exp\left[-(\omega-\omega_j)^2/2\sigma_j^2\right]. \tag{11}$$

Equation (8) may be recast as the overlap of a doorway with a window many-electron functions,[12,31]

$$S_{SXRS}(\tau)=2\mathrm{Re}\,\langle W|D(\tau)\rangle, \tag{12}$$

where the *doorway* state evolves during the delay τ

$$|D(\tau)\rangle = \sum_{g'} D_{g'} e^{-i\omega_{g'g}\tau - \Gamma_{g'}\tau} |g'\rangle, \tag{13a}$$

with (see Appendix B)

$$\begin{aligned} D_{g'} &= \sum_{f_1} V_{g'f_1} V_{f_1 g} \int \frac{d\omega_1}{2\pi} \times \frac{E_1^*(\omega_1) E_1(\omega_1 - \omega_{g'g})}{\omega_1 - \omega_{g'g} - \omega_{f_1 g} + i\Gamma_{f_1}} \\ &= \sum_{f_1} V_{g'f_1} V_{f_1 g} \mathcal{I}_1 \left[\omega_{g'g}, \omega_{f_1 g} + \frac{\omega_{g'g}}{2} + i\Gamma_{f_1} \right] \end{aligned} \tag{13b}$$

$$\mathcal{I}_j \left[\omega_{g'g}, \omega_{f_j g} + \frac{\omega_{g'g}}{2} + i\Gamma_{f_j} \right] = \frac{-\sqrt{2}}{\sigma_j^2} \times \exp\left[\frac{-\omega_{g'g}^2}{4\sigma_j^2} \right] \Delta \left[\left(\omega_{f_j g} + \frac{\omega_{g'g}}{2} - \omega_j + i\Gamma_{f_j} \right) / \sigma_j \right]$$

$$\Delta(z) = e^{-z^2} \left(\frac{\mathrm{Erf}(iz)}{i} - i \right), \tag{13c}$$

where $\{f_j\}$ is the excited state manifold accessible by the jth pulse. The lineshape function $\mathcal{I}_j[\ldots]$ (Ref. 12) is given in Appendix B [Eq. (B12)] and is shown in Fig. 10. The *window* state is

$$|W\rangle = \sum_{g'} W_{g'} |g'\rangle, \tag{14a}$$

with

$$\begin{aligned} W_{g'} &= \sum_{f_2} V_{gf_2} V_{f_2 g'} \int \frac{d\omega_2}{2\pi} \times E_2(\omega_2) E_2^*(\omega_2 - \omega_{g'g}) \\ &\quad \times \mathrm{Im} \frac{1}{\omega_2 - \omega_{g'g} - \omega_{f_2 g} + i\Gamma_{f_2}} \\ &= \sum_{f_2} V_{gf_2} V_{f_2 g'} \mathrm{Im}\, \mathcal{I}_2 \left[\omega_{g'g}, \omega_{f_2 g} + \frac{\omega_{g'g}}{2} + i\Gamma_{f_2} \right]. \end{aligned} \tag{14b}$$

Substituting Eqs. (13) and (14) in Eq. (12) gives

$$S_{\mathrm{SXRS}}(\tau) = \sum_{g' \neq g} D_{g'} W_{g'}^* e^{-i\omega_{g'g}\tau} e^{-\Gamma_{g'}\tau} . + \mathrm{c.c.} \tag{15}$$

We shall display the signal in the frequency domain by performing a Fourier transform with respect to the delay

$$\begin{aligned} S_{\mathrm{SXRS}}(\omega) &\equiv \mathrm{Re} \int_0^\infty \mathrm{d}\tau e^{-i\omega\tau} S_{\mathrm{SR}}(\tau) \\ &= \sum_{g'} \frac{W_{g'}^* D_{g'} \Gamma_{g'}}{(\omega - \omega_{g'g})^2 + \Gamma_{g'}^2}. \end{aligned} \tag{16}$$

III. NATURAL ORBITAL REPRESENTATION OF PARTICLE–HOLE WAVE PACKETS

The expansion of the signal in the many-electron states $|g\rangle$, $|g'\rangle$, and $|f\rangle$ [Eq. (7)] is formally exact. Experimental visualization of the single-particle wave functions (e.g., by using Dyson orbitals) in attosecond high harmonic generation has been reported.[34–36] Below we show how the many-electron wave packet may be represented in real space. We emphasize that this visualization is not directly obtained from experimental data but is derived from simulations and should help the interpretation of experiments. We shall adopt an approximate electronic structure theory in which each state of the valence-excited state manifold with all core orbitals doubly occupied and each state of the core-excited state manifold with a localized core-hole are represented by a single Slater determinant made of ground-state HF orbitals and relaxed orbitals with HF–STEX approximation of the same molecular configuration, respectively. In the STEX computational protocol of the core-excited states $|f\rangle$ described in Appendix C, electronic excitations are treated with respect to different reference states. The more crude ECA simply replaces the atom whose K-edge is resonant with the applied x-ray fields by an atom with the next highest atomic number. The core hole is represented approximately by an extra atomic charge. The STEX model treats the core-excited molecule as a Slater determinant, solved self-consistently with a singly occupied core. Valence excited states from both reference wavefunctions are generated using an independent particle model. This approximation neglects the interaction between the excited electron and its hole, as well as all other electron correlation. The Hamiltonian is taken to be diagonal within the block of singly excited Slater determinants

$$\left\langle \Psi_j^b \middle| \hat{H} \middle|_i^a \Psi \right\rangle = \delta_{ab}\delta_{ij}\omega_{ai}. \tag{17}$$

Within this single-determinant approximation, the reduced doorway-window representation carries the same information as the full many-electron wave packets of the signal, provided the signal is dominated by single-particle excitations

$$|g'\rangle = c_a^\dagger c_i |g\rangle, \tag{18}$$

where $i(a)$ are occupied(unoccupied) valence molecular orbitals and the excitation energy is $\omega_{g'g} = \omega_{ai} = \epsilon_a - \epsilon_i$.

Substituting Eq. (18) in Eqs. (13) and (14), in the molecular orbital basis, the doorway wave packet is given by

$$|D(\tau)\rangle = \sum_i^{\text{occ}} \sum_a^{\text{unocc}} D_{ia} e^{-i\omega_{ai}\tau - \Gamma_{ai}\tau} c_a^\dagger c_i |g\rangle, \tag{19}$$

and the window wave packet is similarly given by

$$|W\rangle = \sum_i^{\text{occ}} \sum_a^{\text{unocc}} W_{ia} c_a^\dagger c_i |g\rangle, \tag{20}$$

D_{ia} and W_{ia} are the expansion coefficients of the particle–hole in these wave packets. Substituting Eqs. (19) and (20) in Eq. (12) gives the SXRS signal in the molecular orbital representation,

$$S_{\text{SXRS}}(\tau) = \sum_i^{\text{occ}} \sum_a^{\text{unocc}} W_{ia} D_{ia} e^{-i\omega_{ai}\tau} e^{-\Gamma_{ai}\tau} + \text{c.c.} \tag{21}$$

A more compact representation and visualization of the doorway wave packet is obtained by using a particle–hole time-dependent basis of natural orbitals (Appendix A). The doorway operator creates a wave packet of valence excitations. The natural orbitals, obtained through a singular value decomposition of the matrix representing this operator, are the most compact representation of the wave packet in terms of single particle → hole excitations. Each particle–hole natural orbital pair has a corresponding positive weight indicating its contribution to the doorway. In this basis the doorway wave packet assumes the form [Eq. (A18)],

$$|D(\tau)\rangle = \sum_\xi d_\xi(\tau) \cdot c_{\xi,p}^\dagger(\tau) c_{\xi,h}(\tau) |g\rangle, \tag{22}$$

where

$$\begin{aligned} c_{\xi,p}^\dagger(\tau) &= \sum_a e^{-i\epsilon_a\tau} c_a^\dagger \chi_{a\xi}^p, \\ c_{\xi,h}(\tau) &= \sum_i \chi_{\xi i}^h c_i e^{i\epsilon_i\tau}, \end{aligned} \tag{23}$$

are the creation and annihilation operators for the time-dependent natural orbitals [see Eq. (A17)]. The coefficients $\chi_{a\xi}^p(\chi_{\xi i}^h)$ are obtained from the particle (hole) parts of the singular value decomposition of the doorway operator at $\tau = 0$.[Eqs. (A12) and (A13)]. The signal is given by the overlap of this wave packet and the window, and is derived in Appendix A [Eq. (A21)]

$$\begin{aligned} S(\tau) &= \sum_\xi w_\xi(\tau) d_\xi(\tau) + \text{c.c.}, \\ w_\xi(\tau) &= \sum_{ai} \chi_{\xi i}^h W_{ia}^* e^{-i\omega_{ai}\tau - \Gamma_{ai}\tau} \chi_{a\xi}^p, \\ d_\xi(\tau) &= \sum_{ai} \chi_{a\xi}^{p*} D_{ai} \chi_{\xi i}^{h*} e^{-\Gamma_{ai}\tau}. \end{aligned} \tag{24}$$

The double sum in Eq. (21) is now replaced by a single sum over orbital pairs. We can visualize the signal by displaying the natural orbitals and the time-dependent product $d_\xi(\tau) w_\xi(\tau)$. When the electronic lifetimes are long compared to the experimental delay time between pulses ($1/\Gamma_{ai} \gg \tau$), the doorway coefficients become time independent, $d_\xi(\tau) \equiv d_\xi$.

The natural orbital basis places the doorway in the Schmidt representation,[37] and partitions the time evolution in the system so that $d_\xi(\tau)$ is controlled by the lifetimes, and $w_\xi(\tau)$ contains the valence excitation frequencies in the response. Graphing the time-dependent signal as the product of these two functions will allow us to dissect it in terms of these separate contributions.

IV. XANES SPECTRA OF NMA: ORBITAL RELAXATION AT THE ECA AND STEX LEVELS

The geometry of *trans*-NMA (C_3H_6NHO, see Fig. 3) was optimized using density functional theory and the GAUSSIAN03 (Ref. 38) code at the B3LYP/6-311G** level. The ECA calculations were carried on using GAUSSIAN03, while the STEX calculations were implemented using PSI3.[39] All transition frequencies and dipole moments were calculated at the HF/6-311G** level. The ECA and STEX frontier orbital energies are compared in Table I (Table II) for core electronic excitation from N1s(O1s) orbital. In ECA, the core-excited state is calculated using an additional electron in the valence band. For NMA, the STEX procedure results in a LUMO where this extra electron is bound (orbital with negative energy); all other virtual orbitals have positive energies. STEX predicts additional bound virtual orbitals (i.e., LUMO+0, 1, 2 for N K-edge and LUMO+0, +1 for the O K-edge), due to the improved description of orbital relaxation in the core-hole field. Glycine is the amino-acid which most resembles *trans*-NMA. The low-temperature experimental XANES spectra for a crystal of glycine (Fig. 3, bottom, see Ref. 40) contain features within 3–5 eV of the core absorption edge, as seen in our STEX simulations.

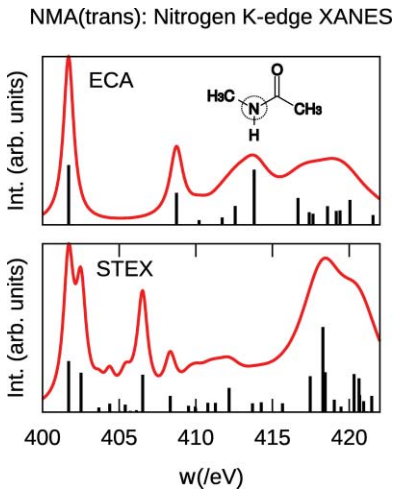

FIG. 3. XANES N1s spectra [Eq. (25)] computed at the ECA and STEX levels. The stick spectra were convoluted with a Lorentzian, with a constant linewidth (fwhm) of 0.4 until 408 eV. It was then increased linearly to 1.5 eV between 408 and 415 eV, and held constant at this value for higher energies.

TABLE I. Energies (in hartree) of the frontier molecular orbitals upon N1*s* core electronic excitation.

Orbital	ϵ_{gs}^{HF}	ϵ_{ex}^{ECA}	ϵ_{ex}^{STEX}
HOMO-3	−0.54280	−0.53851	0.76604
HOMO-2	−0.50228	−0.52685	−0.76183
HOMO-1	−0.41550	−0.48208	−0.69517
HOMO	−0.38687	−0.37305	0.67413
LUMO	0.14066	−0.17241	−0.07778
LUMO+1	0.16963	0.08626	−0.04795
LUMO+2	0.18882	0.14036	−0.00561
LUMO+3	0.19405	0.18858	0.02078

The energy difference between the highest occupied molecular orbital (HOMO) and LUMO orbitals in *trans*-NMA are 5.45 eV, a similar bandgap exists in core-excited glycine. The decreased energy separation of the STEX orbitals allows core-excited spectra to be described as single excitations in a one-particle picture, and match peaks near the absorption edge.

We start with the simulated XANES spectra

$$S_{\mathrm{XANES}}(\omega) = \frac{1}{\pi} \sum_f \frac{|\mu_{fg}|^2 \Gamma_f}{(\omega - \omega_{fg})^2 + \Gamma_f^2}, \tag{25}$$

where μ_{fg} is the transition dipole between the ground state g and core-excited states f. For the lifetime broadening, due to autoionization lifetimes from valence-excited states we used the following values: $\Gamma_{f_N} = 0.4$ eV for energies up to 408 eV for N1*s* and linearly ramped to 1.5 eV at 415 eV and held constant, and $\Gamma_{f_O} = 0.4$ eV at 537 eV and ramped to 1.5 eV at 544 eV for O1*s* core-excited states. The first XANES transition was set to 401.7 eV for nitrogen and 532.0 eV for oxygen to match experiment.[41] Atomic x-ray photoemission linewidths for nitrogen (0.09 eV) and oxygen (0.133 eV) imply a core-hole lifetime of 7.3 and 4.9 fs respectively. Both linewidths are taken from LLNL EADL library for atomic cross-sections.[42] Molecular NEXAFS and XANES linewidths will likely be larger, each molecule will have a slightly different environment local to the core. These widths will not reflect a core-hole decay time, which is a single molecule property, but an inhomogeneous distribution of transition frequencies,

TABLE II. Energies (in hartree) of the frontier molecular orbitals upon O1*s* core electronic excitation.

Orbital	ϵ_{gs}^{HF}	ϵ_{ex}^{ECA}	ϵ_{ex}^{STEX}
HOMO-3	−0.54280	−0.55594	−0.78115
HOMO-2	−0.50228	−0.54143	−0.76318
HOMO-1	−0.41550	−0.50446	−0.75076
HOMO	−0.38687	−0.45016	−0.65531
LUMO	0.14066	−0.21724	−0.09095
LUMO+1	0.16963	0.14950	−0.03607
LUMO+2	0.18882	0.17435	0.00986
LUMO+3	0.19405	0.20133	0.02272

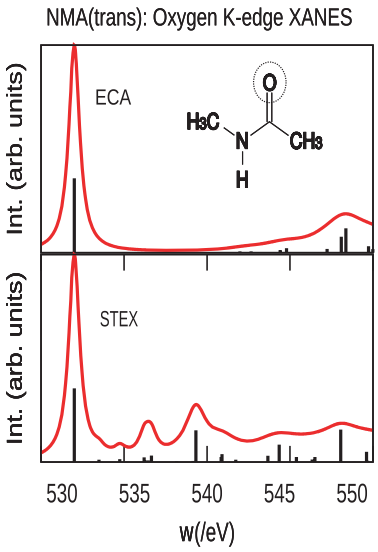

FIG. 4. XANES O1*s* spectra [Eq. (25)] computed at the ECA and STEX levels. The stick spectra were convoluted with a Lorentzian, with a constant linewidth of 0.4 eV until 537 eV, and then increased linearly to 1.5 eV from 537 to 544 eV, and held constant at this value for higher energies.

a property of the sampled ensemble. We do not address any averaging over nuclear configurations or environments in our simulations. We include these effects approximately by using a linewidth which was used to match the experimental XANES of small organic molecules in previous studies.[12,23] The increased linewidth represents bound resonances coupled to a continuum of photoelectron states; since our focus is on Raman-type inelastic scattering processes occurring on a short time scale, and since our pulse bandwidth extends only weakly into this region of the core-excited density of states, a higher level simulation strategy of ionized states was not adopted.

The fluorescence yield for both the oxygen and nitrogen core-holes is below 1%.[43] For soft x-ray core-excitations in the light elements, the frequency difference between the K and L x-ray edges is much larger than between the 2*s* orbital and the ionization potential. Conservation of energy leads to a dominant Auger shake-off rather than shake-up spectra. Therefore, the initial pump excitation may create an ionized state during the delay period, formed by Auger decay. An implicit assumption made in the present work is that the probe core–hole transitions for the ionized molecule are detuned from the neutral transitions by much larger energies than the probing pulse bandwidth, making the SXRS technique selective for neutral molecules evolution during the delay τ. The difference between the first and second ionization energies is usually ∼100 eV, but the core edge for differently ionized species may not be shifted by a similar amount. If this condition does not hold, then ionized species could contribute to the response and must be included.

The XANES spectra obtained using the ECA and STEX levels of core excitations are shown in Fig. 3 for the N K-edge and Fig. 4 for the O K-edge excitations. STEX reveals additional low-energy peaks adjacent to the core edge in both figures, reflecting the relaxation effect of the occupied orbitals

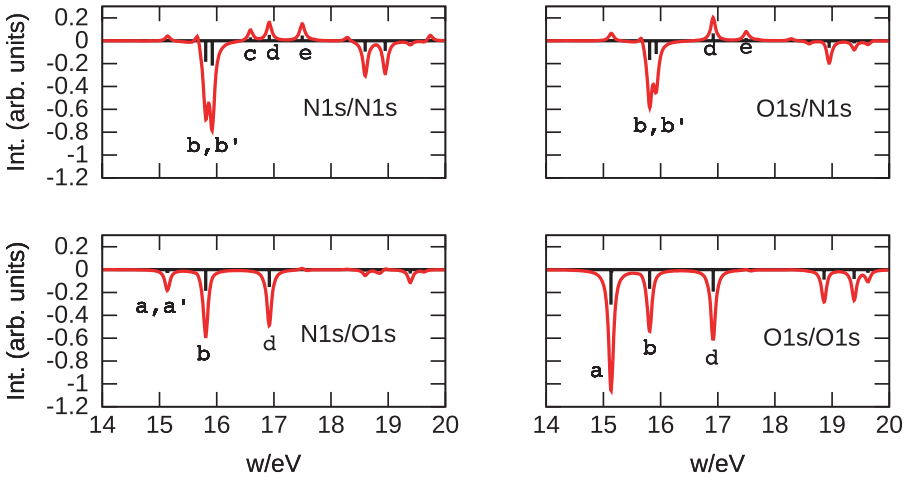

FIG. 5. Stimulated Raman spectra [Eq. (16)] for the four possible pump/probe pulse configurations [Eq. (15)], for peak assignment, see Table III and Fig. 6. Signal intensities $S(\tau)$ are convoluted with Lorentzians with $\Gamma = 0.05$ eV.(0.10 eV fwhm) ($\Gamma_{g'} = \Gamma_{ai} = 0.05$ eV.)

and its improved description of the virtual orbitals. The first XANES peak corresponds to an x-ray transition between the ground and core-excited reference states (no valence excitation). The ECA N K-edge XANES energy difference between the initial core edge at 401.7 eV and the next peak at 408.7 eV is ~ 7.0 eV. STEX predicts a much smaller 0.8 eV peak splitting. The reason for this additional low energy structure is the improved description of the low-lying virtual orbitals in the STEX technique. The HOMO–LUMO splitting is 0.25867 hartrees ~ 7.0 eV as shown in Table I. Whereas the ECA model used here is essentially a Hartree–Fock calculation with modified nuclear and electronic configurations, and typically overestimates the energy gap between HOMO and LUMO. Similar trends are seen in the XANES spectra for the O K-edge excitation, shown in Fig. 4.

V. SXRS SIGNALS OF NMA

We have assumed Gaussian pulses in Eq. (5) with $\sigma_j = 77$ as. Since the pulse central frequency is tuned to the core edge, only half of the 20.13 eV bandwidth ($\propto 1/\sigma_j$) is available for an x-ray Raman process; giving an effective 10.07 eV pulse bandwidth. The core-hole linewidths used for Eq. (8) are $\Gamma_{f_N} = 0.085$ eV for N1s and $\Gamma_{f_O} = 0.10$ eV for O1s, and the linewidth of valence-excited states is $\Gamma_{g'} = 0.05$ eV. The frequency domain SXRS signal was calculated by taking the Fourier transform of Eq. (21)

$$S_{\mathrm{SXRS}}(\omega) = \frac{1}{\pi} \sum_{i}^{\mathrm{occ}} \sum_{a}^{\mathrm{unocc}} \frac{W_{ai} D_{ai} \Gamma_{ai}}{(\omega \pm \omega_{ai})^2 + \Gamma_{ai}^2}. \tag{26}$$

The signal at $\omega_{g'g}$ is proportional to $W^*_{g'} D_{g'}$. Figure 5 shows the stimulated Raman signals for N1s pump/N1s probe ($\omega_1 = \omega_2 = \omega_N$), N1$s$ pump/O1s probe($\omega_1 = \omega_N, \omega_2 = \omega_O$), O1$s$ pump/N1s probe($\omega_1 = \omega_O, \omega_2 = \omega_N$), and O1$s$ pump/O1s probe($\omega_1 = \omega_2 = \omega_O$). The large HOMO–LUMO splitting in the ground state pushes the lowest energy single excitations into higher energies. The small 0.05 eV broadening for the valence excited states may not apply if the inverse of the autoionization rate for an electron excited to a state competes with the delay time between pulses. Additional work is needed to quantify the interaction between these processes.

The O1s/O1s (oxygen pump/ oxygen probe) signal shows a strong negative transition(a) near 15.13 eV corresponding to an excitation from an orbital with π character on the oxygen to a σ^* state on the non-adjacent methane (Fig. 6). Neither orbital is localized on the nitrogen, and neither of the nitrogen doorway or window operators have a significant dipole matrix element for this transition. The N1s/O1s spectrum has a transition in the same frequency range, which is a combination of the (a) transition, and another π to σ^* transition to the methyl-group adjacent to the oxygen. The

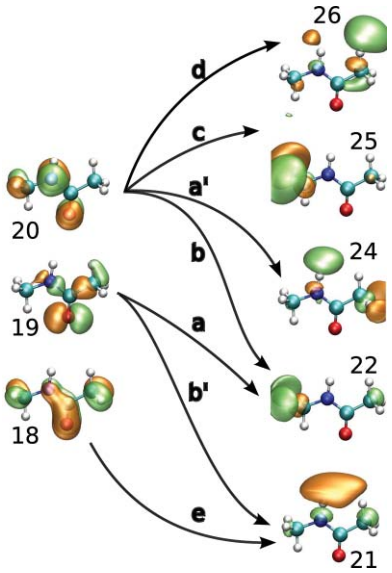

FIG. 6. Peak assignment for SXRS transitions (see Table III).

transition (b) at 15.81 eV makes significant contribution to all four signals. In comparison with transition (a), (b) comes from an excitation from an occupied π orbital delocalized over nitrogen *and* oxygen to the σ^* orbital on nitrogen's adjacent methyl group. For the techniques with a nitrogen window, (b′) also contributes. The three states (c) at 16.59 eV, (d) at 16.92 eV, and (e) at 17.50 eV contribute positive peaks to the nitrogen probe spectra, and negative absorptive peaks to the oxygen SXRS signal. The absorptive peaks are due to the sign of the doorway and window operators for the nitrogen, which are the same for this particular transition.

The time-resolved SXRS signal is shown in Fig. 7. Since the splitting between the states comprising the electronic wave packet is small compared to their mean frequency, they do not evolve much phase in approximately one period. The signal will be analyzed using the doorway natural orbitals. We choose a real basis of molecular orbitals, and for $\tau = 0$, the natural orbitals which are linear combinations of these are also real (see Appendix A). In Figs. 8 and 9 we display the doorway natural orbitals at $\tau = 0$ for a pulse tuned to the nitrogen and oxygen 1*s* core transitions, respectively. The weights $d_{1\ldots5}(\tau)$ [Eq. (A18)] are shown in the left column of the same figure. These represent the strengths of the contribution of each particle-hole pair to the doorway.

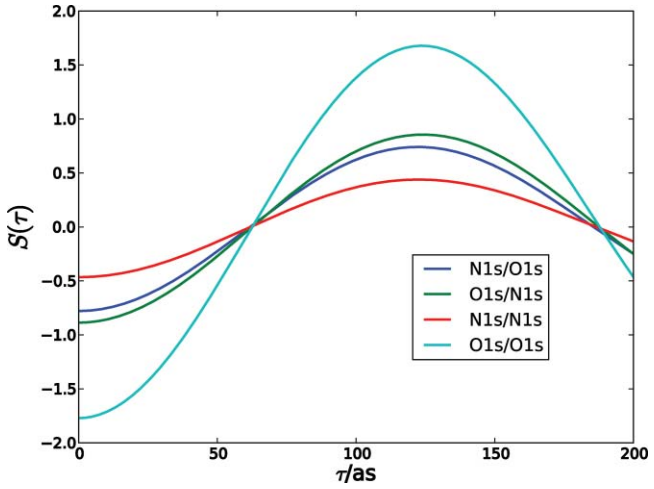

FIG. 7. Time-dependent SXRS signal for NMA for different pump/probe configurations, as indicated.

Displaying the natural orbitals as a function of the delay time τ provides a real space movie of the evolving wave

TABLE III. SXRS signal decomposition for each excitation. Column (a) is the excitation number: excitation #1 corresponds to Raleigh scattering of the pump pulse and contributes a time-independent, DC contribution to the signal as a function of pulse delay which is neglected. Columns (b) and (c) represent the orbitals contributing to the excitation, with a frequency given in Column (d). Columns (e–h) are the doorway and window amplitudes for pulses tuned to the nitrogen and oxygen core edges, and Columns (i–l) are the signals calculated using these amplitudes, at the frequencies ω_{ai}.

Ex. #	From orb. (i)	To orb (a)	ω_{ai}(/eV)	D^N_{ia}	W^N_{ia}	D^O_{ia}	W^O_{ia}	$S^{NN}(\omega_{ai})$	$S^{NO}(\omega_{ai})$	$S^{ON}(\omega_{ai})$	$S^{OO}(\omega_{ai})$
1	0	0	0.00000	−3.158	11.020	−1.838	1.714	–	–	–	–
2	20	21	14.35505	0.002	−0.008	−0.066	−0.006	−1.742e-05	−1.334e-05	5.241e-04	4.014e-04
3(a)	19	21	15.13399	−0.046	−0.018	−0.501	0.612	8.538e-04	−2.833e-02	9.235e-03	−3.064e-01
4(a′)	20	22	15.14331	−0.154	−0.087	−0.141	0.186	1.347e-02	−2.870e-02	1.235e-02	−2.632e-02
5	20	23	15.66540	−0.300	−0.126	−0.215	−0.023	3.796e-02	6.934e-03	2.723e-02	4.974e-03
6(b)	20	24	15.80789	−0.413	0.448	−0.375	0.450	−1.852e-01	−1.857e-01	−1.682e-01	−1.687e-01
7(b′)	19	22	15.92226	−0.305	0.714	−0.164	−0.018	−2.181e-01	5.371e-03	−1.169e-01	2.879e-03
8	19	23	16.44434	−0.000	0.001	−0.001	0.001	−6.531e-07	−6.107e-07	−1.572e-06	−1.471e-06
9	19	24	16.58683	−0.032	−0.013	−0.000	−0.000	4.197e-04	2.032e-06	5.918e-07	2.865e-09
10(c)	20	25	16.59096	−0.266	−0.112	−0.001	0.001	2.987e-02	−3.796e-04	8.140e-05	−1.034e-06
11(d)	20	26	16.91952	−0.323	−0.157	−0.408	0.476	5.058e-02	−1.536e-01	6.387e-02	−1.939e-01
12	19	25	17.36990	−0.000	0.001	0.001	−0.002	−5.809e-08	1.870e-07	5.983e-07	−1.926e-06
13	20	27	17.44763	0.000	0.000	−0.000	0.000	5.177e-09	4.818e-10	−3.340e-09	−3.108e-10
14(e)	18	21	17.49549	−0.304	−0.150	−0.159	−0.017	4.576e-02	5.234e-03	2.387e-02	2.731e-03
15	20	28	17.57582	−0.066	−0.044	−0.072	0.044	2.877e-03	-2.866e-03	3.153e-03	−3.141e-03
16	19	26	17.69846	−0.055	−0.025	−0.074	−0.008	1.398e-03	4.506e-04	1.874e-03	6.038e-04
17	19	27	18.22658	0.002	−0.008	0.002	−0.002	−1.457e-05	−3.115e-06	−1.207e-05	−2.581e-06
18	18	22	18.28376	−0.155	−0.076	−0.077	−0.009	1.176e-02	1.463e-03	5.866e-03	7.298e-04
19	19	28	18.35476	0.000	0.000	−0.045	−0.005	6.213e-08	−1.789e-06	−7.700e-06	2.217e-04
20	17	21	18.59790	−0.431	0.222	−0.036	0.037	−9.553e-02	−1.579e-02	−7.871e-03	−1.301e-03
21	18	23	18.80584	−0.080	−0.035	−0.043	0.043	2.824e-03	-3.450e-03	1.517e-03	−1.853e-03
22	16	21	18.85959	−0.034	−0.015	−0.349	0.252	5.010e-04	−8.481e-03	5.202e-03	−8.806e-02
23	18	24	18.94833	−0.249	0.358	−0.175	−0.019	−8.927e-02	4.616e-03	−6.279e-02	3.247e-03
24	17	22	19.38616	−0.139	0.074	−0.323	0.255	−1.030e-02	−3.556e-02	−2.388e-02	−8.242e-02
25	15	21	19.58259	−0.025	0.032	−0.025	−0.003	−7.955e-04	6.963e-05	−7.934e-04	6.945e-05
26	20	29	19.62674	−0.033	0.045	−0.183	0.165	−1.465e-03	−5.418e-03	−8.124e-03	−3.005e-02
27	16	22	19.64785	−0.095	0.039	−0.025	−0.003	−3.735e-03	2.958e-04	−9.736e-04	7.711e-05
28	18	25	19.73140	−0.048	−0.016	−0.078	−0.008	7.404e-04	3.750e-04	1.209e-03	6.126e-04
29	14	21	19.73546	−0.180	−0.088	−0.009	−0.001	1.586e-02	9.297e-05	7.717e-04	4.524e-06
30	17	23	19.90824	0.001	0.000	0.001	−0.000	2.170e-07	−2.358e-07	2.144e-07	−2.330e-07

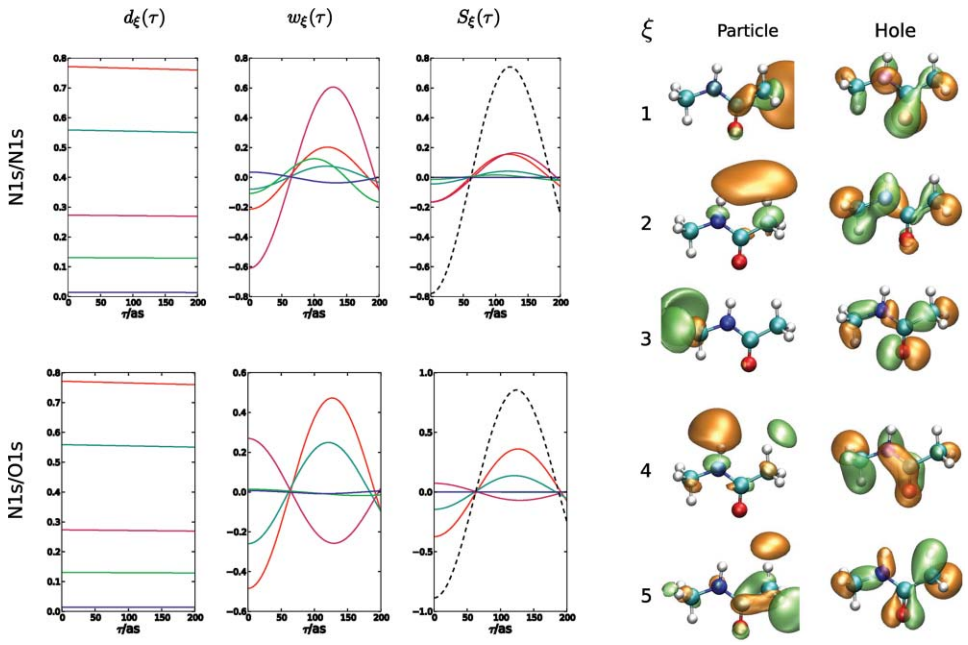

FIG. 8. Time-dependent SXRS signal for NMA for a pump tuned to the nitrogen K-edge, decomposed into contributions from: (first col) the time-dependent doorway weight for each natural orbital, (second col) the projection of the window operator onto each doorway natural orbital, and (third col) the contribution to the signal for each product: $S_\xi = 2Re\, d_\xi(\tau)w_\xi(\tau)$. The dashed black line is the total signal $S_{\rm tot}(\tau) = \sum_\xi S_\xi(\tau)$. (Right) Nitrogen 1$s$ doorway operator natural orbitals at $\tau = 0$.

function created by the pump. Since natural orbitals are linear combinations of delocalized molecular orbitals, it is not easy to correlate the signal with charge migration between the atoms resonant with each pulse, particularly for a small molecule such as NMA.

To trace the origin of the signal, we have dissected it into individual doorway natural orbital contributions. The four possible pump/probe signals (N1s/O1s, N1s/N1s, O1s/N1s and O1s/O1s) for the time-interval τ between 0 to 200 as are shown in Figs. 8 and 9, along with their decomposition in terms of $d_\xi(\tau)$ and $w_\xi(\tau)$. In the N1s/N1s spectra, the first and the third doorway natural orbitals contribute most strongly to the response. Both have π hole character local to the nitrogen atom, and particle orbitals localized on one of the two methyl groups. In the N1s/O1s spectra, the second and the third natural orbital contributions are out of phase, and nearly cancel. The signal is mainly due to the first natural orbital. The three peaks have diffuse particle states, and hole states delocalized over the nitrogen and oxygen atoms. Similar trends are observed for the O1s/N1s and O1s/O1s spectra.

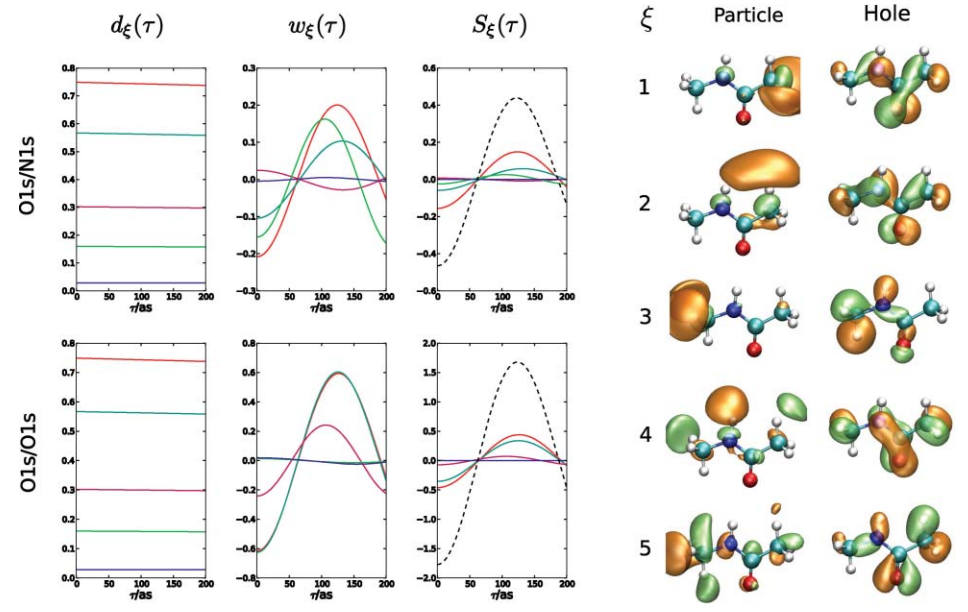

FIG. 9. Time-dependent SXRS signal for NMA for a pump tuned to the oxygen K-edge, decomposed into contributions from: (first col) the time-dependent doorway weight for each natural orbital, (second col) the projection of the window operator onto each doorway natural orbital, and (third col) the contribution to the signal for each product: $S_\xi = 2Re\, d_\xi(\tau)w_\xi(\tau)$. The dashed black line is the total signal $S_{\rm tot}(\tau) = \sum_\xi S_\xi(\tau)$. (Right) Nitrogen 1$s$ doorway operator natural orbitals at $\tau = 0$.

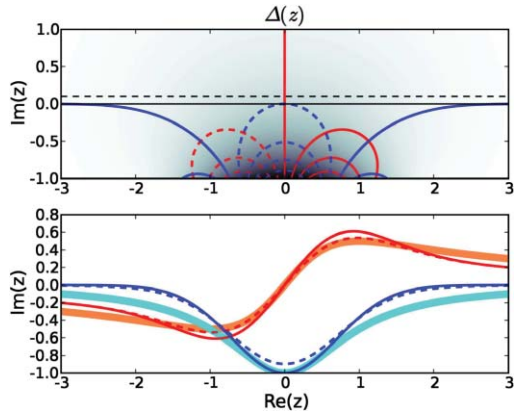

FIG. 10. Top: Real (red) and imaginary (blue) parts of the function $\Delta(z)$ [Eq. (B7)], shaded by $|\Delta(z)|$. Bottom: a slice through $\Delta(x)$ for real argument x(solid), $\Delta(x+0.1i)$ (dashed) compared to the real (orange) and imaginary (cyan) parts of the function $1/(x+i)$.

VI. CONCLUSIONS

There are three time scales governing the evolution of a core-excited system, the nuclear motion, and the valence and core electronic degrees of freedom. We have performed a qualitative simulation neglecting nuclear motion and including the core-hole valence electron coupling through the STEX approximation. Excitations within the valence band were described in a simple one-particle scheme, neglecting the influence of the hole on an excited particle. More sophisticated methods exist for treating electron correlation, including the Bethe–Salpeter,[44] algebraic diagrammatic construction,[45] CI, and coupled-cluster methods[46] for calculating excited valence eigenstates. Many improvements in the level of theory used to treat nuclear motion, electron correlation in excited states, and the core–hole/valence coupling will be needed to accurately simulate core-excited nuclear and electronic dynamics.

We have simulated the SXRS spectra of the nitrogen and oxygen K-edges in *trans*-NMA by treating the core-excitations at the Hartree–Fock static-exchange level. Compared with the equivalent-core approximation, in which the core-hole potential is described as a positive charge, STEX predicts the correct spin symmetry of the excited states and provides an improved description for both the occupied and virtual orbitals. The STEX N1*s* and O1*s* XANES spectra shows additional peaks that are missed by the ECA calculations. The SXRS signal was expressed as an overlap between the doorway and window wave packets. The valence electron-hole dynamics is followed by monitoring the changes in the particle–hole orbital pairs, using a compact natural orbital representation.

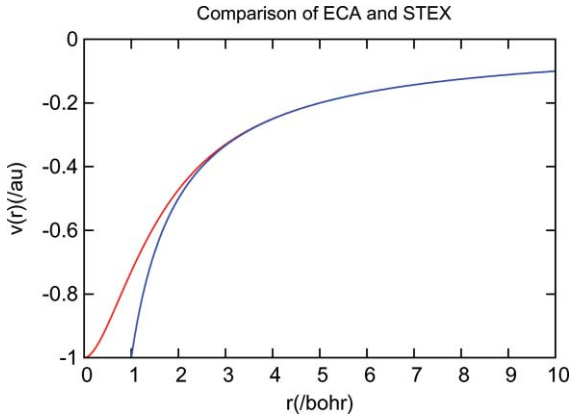

FIG. 11. $v_c(\mathbf{r})$ (red-solid, see Eq. (D3)) and $v_{\mathrm{ECA}}(\mathbf{r})$ (blue, $-1/r$) as a function of radial distance from the resonant core-atom. All values in atomic units, with $\alpha = 1$.

ACKNOWLEDGMENT

The support of the Chemical Sciences, Geosciences and Biosciences Division, Office of Basic Energy Sciences, Office of Science, (U.S.) Department of Energy (DOE) is gratefully acknowledged.

APPENDIX A: THE TIME-DEPENDENT NATURAL ORBITAL BASIS SET

The signal [Eq. (21)] can be recast in terms of the product of two block off-diagonal matrices in the electron and hole blocks,

$$S(\tau) = \mathrm{Re}\,\mathrm{Tr}\left[\mathbf{W}^{\mathbf{T}}\mathbf{D}(\tau)\right], \tag{A1}$$

$$\mathbf{D}(\tau) = \begin{bmatrix} \mathbf{0} & & \mathbf{0} \\ D_{l1}e^{-i\omega_{l1}\tau-\Gamma_{l1}\tau} & \cdots & D_{lh}e^{-i\omega_{lh}\tau-\Gamma_{lh}\tau} \\ \vdots & \ddots & \vdots \\ D_{n1}e^{-i\omega_{n1}\tau-\Gamma_{n1}\tau} & \cdots & D_{nh}e^{-i\omega_{nh}\tau-\Gamma_{nh}\tau} \end{bmatrix} \begin{matrix} \\ \\ \\ \mathbf{0} \end{matrix}$$

$$\mathbf{W} = \begin{bmatrix} \mathbf{0} & & \mathbf{0} \\ W_{l1} & \cdots & W_{lh} \\ \vdots & \ddots & \vdots \\ W_{n1} & \cdots & W_{nh} \end{bmatrix} \begin{matrix} \\ \\ \\ \mathbf{0} \end{matrix}, \tag{A2}$$

where $D_{lh}(W_{lh})$ is the doorway (window) weight corresponding to the HOMO $\rightarrow$ LUMO transition and n is the total number of orbitals. The doorway and window wave packets will be represented using the basis set of the natural orbitals.[12,33,47] This is a more compact representation than the molecular orbitals since only a few natural orbital pairs are typically required. The matrices in Eq. (A2) do not commute with their adjoints and cannot be diagonalized. However, they can be transformed using the single value decomposition algorithm. Any matrix (not necessarily square) can be recast in the form,[48]

$$\begin{aligned} \mathbf{D} &= \mathbf{X}^{p}\Sigma\mathbf{X}^{h\,\dagger}, \\ D_{ai} &= \sum_{\xi} \chi^{p}_{a\xi} d_{\xi} \chi^{h}_{\xi i}, \end{aligned} \tag{A3}$$

where $\mathbf{X}^p$ and $\mathbf{X}^h$ are unitary matrices with elements

$$(\mathbf{X}^{p})_{a\xi} = \chi^{p}_{a\xi}, \tag{A4}$$

$$(\mathbf{X}^{h\,\dagger})_{\xi i} = \chi^{h}_{\xi i}, \tag{A5}$$

and $\mathbf{\Sigma}$ is a diagonal matrix with real, positive matrix elements d_ξ. If the diagonal elements of $\mathbf{\Sigma}$ are sorted in a fixed order, the decomposition in Eq. (A3) is unique, up to a unitary complex factor $e^{i\theta_\xi}$ for each of the rows of $\mathbf{X}^p$ and $\mathbf{X}^h$.

The rows of the matrix $\mathbf{X}^p$ and the columns of $\mathbf{X}^{h\dagger}$ are the *particle and hole natural orbitals* corresponding to the doorway operator. The operator can be written in a diagonal form

$$\mathbf{\Sigma} = \mathbf{X}^{p\dagger}\mathbf{D}\mathbf{X}^h \tag{A6}$$

with

$$d_\xi = \sum_{ai} \chi^{p*}_{a\xi} D_{ai} \chi^h_{\xi i}. \tag{A7}$$

One important consequence of the uniqueness of the singular value decomposition is that $\mathbf{\Sigma}$ is invariant under a unitary transformation of $\mathbf{D}$. Let $\mathbf{O}$ be a unitary matrix. Since the product of two unitary matrices is unitary,

$$\begin{aligned}\mathbf{O}\mathbf{D}\mathbf{O}^\dagger &= \mathbf{O}\mathbf{X}^p\mathbf{\Sigma}\mathbf{X}^{h\dagger}\mathbf{O}^\dagger \\ &= \tilde{\mathbf{X}}^p\mathbf{\Sigma}\tilde{\mathbf{X}}^{h\dagger},\end{aligned} \tag{A8}$$

where

$$\tilde{\mathbf{X}}^p = \mathbf{O}\mathbf{X}^p, \qquad \tilde{\mathbf{X}}^h = \mathbf{O}\mathbf{X}^h. \tag{A9}$$

We assume that the electronic lifetime Γ^{-1}_{ai} in Eq. (19) is long compared to the delay between the x-ray pulses making the time evolution of the doorway operator unitary on the experimental time scale. Then the time evolution of the doorway operator is a unitary transformation,

$$\mathbf{D}(\tau) \simeq e^{-i\mathbf{H}\tau} D(0) e^{i\mathbf{H}\tau}, \tag{A10}$$

where the matrix,

$$\mathbf{H}_{rs} = \delta_{rs}\epsilon_r, \tag{A11}$$

represents the single particle Hartree–Fock Hamiltonian. Using the natural orbitals of the doorway operator as a basis set, the time dependent singular value decomposition [using $\mathbf{O} = e^{-i\mathbf{H}\tau}$ in Eq. (A9)] is

$$(\mathbf{X}^p(\tau))_{a\xi} = \chi^p_{a\xi} e^{-i\epsilon_a\tau}, \tag{A12}$$

$$(\mathbf{X}^{h\dagger}(\tau))_{\xi i} = \chi^h_{\xi i} e^{i\epsilon_i\tau}. \tag{A13}$$

Inserting factors of $\mathbf{X}^p\mathbf{X}^{p\dagger}$ and $\mathbf{X}^h\mathbf{X}^{h\dagger}$ into Eq. (A1), the signal $S(\tau)$ can be written in this representation,

$$\begin{aligned}S(\tau) &= 2\mathrm{Re}\,\mathrm{Tr}[\mathbf{W}^{\mathbf{T}}\mathbf{D}(\tau)] \\ &= 2\mathrm{Re}\,\mathrm{Tr}[\mathbf{W}^{\mathbf{T}}\mathbf{X}^p(\tau)\mathbf{X}^{p\dagger}(\tau)\mathbf{D}\mathbf{X}^h(\tau)\mathbf{X}^{h\dagger}(\tau)]\end{aligned} \tag{A14}$$

$$= 2\mathrm{Re}\sum_\xi w_\xi(\tau) d_\xi(\tau), \tag{A15}$$

where the diagonal part of the window operator,

$$\begin{aligned}w_\xi(\tau) &= \langle c^\dagger_\xi(\tau) c_\xi(\tau)|W\rangle = (\mathbf{X}^{h\dagger}(\tau)\mathbf{W}^\dagger\mathbf{X}^p(\tau))_{\xi,\xi} \\ &= \sum_{ai} \chi^{h*}_{\xi i} W^*_{ai} \chi^p_{a\xi} e^{-i\omega_{ai}\tau},\end{aligned} \tag{A16}$$

where $w_\xi \equiv w_{\xi\xi}(\tau)$ is the diagonal part of the window operator in the doorway natural orbital representation. Equation (A14) can be derived using an operator formalism. The time-dependent creation and annihilation operators for the doorway particle and hole orbitals are defined as

$$\begin{aligned}c^\dagger_{\xi p}(\tau) &= \sum_a e^{-i\epsilon_a\tau} c^\dagger_a \chi^p_{a\xi}, \\ c_{\xi h}(\tau) &= \sum_i \chi^h_{\xi i} e^{i\epsilon_i\tau} c_i,\end{aligned} \tag{A17}$$

to make the doorway and window wave packets in the new basis

$$\begin{aligned}|D(\tau)\rangle &= \sum_\xi d_\xi(\tau) c^\dagger_{\xi,p}(\tau) c_{\xi,h}(\tau)|g\rangle, \\ |W\rangle &= \sum_{\xi',\xi''} w_{\xi',\xi''}(\tau) c^\dagger_{\xi',p}(\tau) c_{\xi'',h}(\tau)|g\rangle, \\ d_\xi(\tau) &= \sum_{ai} \chi^{p*}_{a\xi} D_{ai} \chi^h_{\xi i} e^{-\Gamma_{ai}\tau}, \\ w_{\xi'\xi''}(\tau) &= \sum_{ai} \chi^{h*}_{\xi' i} W^*_{ai} \chi^p_{a\xi''} e^{-i\omega_{ai}\tau},\end{aligned} \tag{A18}$$

match their original definitions

$$\begin{aligned}|D(\tau)\rangle &= \sum_{ai} D_{ia} e^{-i\omega_{ai}\tau - \Gamma_{ai}\tau} c^\dagger_a c_i|g\rangle, \\ |W\rangle &= \sum_{ai} W_{ia} c^\dagger_a c_i|g\rangle.\end{aligned} \tag{A19}$$

The signal is recast as the time-dependent overlap between these two wave packets. In the independent particle approximation presented in Appendix C, particles and holes are not coupled to each other, the electron and hole natural orbitals of the doorway remain linear combinations of virtual and occupied orbitals, and the operators in Eq. (A14) can be factored into separate contributions. When the ground state is written as an outer product of a set of occupied orbitals and a vacuum of unoccupied orbital states,

$$|g\rangle = |\mathbf{1}_{\mathrm{occ}}\rangle \otimes |\mathbf{0}_{\mathrm{unocc}}\rangle, \tag{A20}$$

the creation and annihilation operators defined in Eq. (A17) only act on one of the subspaces, and the signal can be factored

$$S(\tau) = \langle W|D(\tau)\rangle, \tag{A21}$$

$$S(\tau) = \sum_{\xi,\xi'\xi''} w^*_{\xi'\xi''}(\tau) d_\xi(\tau) \langle g|c^\dagger_{\xi'' h}(\tau) c_{\xi' p}(\tau) c^\dagger_\xi(\tau) c_\xi(\tau)|g\rangle$$

$$= \sum_{\xi,\xi'\xi''} w^*_{\xi'\xi''}(\tau) d_\xi(\tau) \langle \mathbf{1}_{\mathrm{occ}}|c^\dagger_{\xi'' h}(\tau) c_{\xi h}(\tau)|\mathbf{1}_{\mathrm{occ}}\rangle \langle \mathbf{0}_{\mathrm{unocc}}|c_{\xi' p}(\tau) c^\dagger_{\xi p}(\tau)|\mathbf{0}_{\mathrm{unocc}}\rangle,$$

$$\langle \mathbf{1}_{\rm occ}|c^\dagger_{\xi'' h}(\tau)c_{\xi h}(\tau)|\mathbf{1}_{\rm occ}\rangle = \sum_{ij}\chi^h_{\xi j}\chi^{h*}_{\xi'' i}\langle \mathbf{1}_{\rm occ}|c^\dagger_i c_j|\mathbf{1}_{\rm occ}\rangle e^{-i\omega_{ij}\tau} = \sum_{ij}\chi^h_{\xi j}\chi^{h*}_{\xi'' i}\delta_{ij}e^{-i\omega_{ij}\tau} = \sum_i \chi^h_{\xi i}\chi^{h*}_{\xi'' i} = \delta_{\xi''\xi}, \tag{A22}$$

$$\langle \mathbf{0}_{\rm unocc}|c_{\xi' p}(\tau)c^\dagger_{\xi p}(\tau)|\mathbf{0}_{\rm unocc}\rangle = \sum_{ab}\chi^{p*}_{\xi' a}\chi^p_{\xi b}\langle \mathbf{0}_{\rm unocc}|c_a c^\dagger_b|\mathbf{0}_{\rm unocc}\rangle e^{-i\omega_{ba}\tau} = \sum_{ab}\chi^{p*}_{\xi' a}\chi^p_{\xi b}\delta_{ab}e^{-i\omega_{ba}\tau} = \sum_a \chi^{p*}_{\xi' a}\chi^p_{\xi a} = \delta_{\xi'\xi}, \tag{A23}$$

where the orthonormality of the natural orbitals (unitary $\mathbf{X}^{p,h}$) has been used. The final expression for the signal is

$$\begin{aligned} S(\tau) &= 2{\rm Re}\sum_{\xi\xi'\xi''} w_{\xi'\xi''}(\tau)d_\xi(\tau)\delta_{\xi''\xi}\delta_{\xi'\xi} = 2{\rm Re}\sum_\xi w_\xi(\tau)d_\xi(\tau), \\ w_\xi(\tau) &= \sum_{ai}\chi^h_{\xi i}W^*_{ia}e^{-\omega_{ai}\tau}\chi^p_{a\xi}, \\ d_\xi(\tau) &= \sum_{ai}\chi^{p*}_{a\xi}D_{ai}\chi^{h*}_{\xi i}e^{-\Gamma_{ai}\tau}. \end{aligned} \tag{A24}$$

Only the diagonal part of the transformed window operator in the doorway natural orbital representation contributes to the SXRS signal.

APPENDIX B: THE DOORWAY AND THE WINDOW WAVE PACKETS FOR GAUSSIAN PULSES

The integral describing how the pump-probe pulse shapes weight material transition frequencies is a convolution of the field over the response function. It is a sum over $|e\rangle$ of terms

$$\int_{-\infty}^{\infty}\frac{{\rm d}\,\omega}{2\pi}\frac{E^*_j(\omega)E_j(\omega-\omega_{fg})}{\omega-\omega_{fg}-\omega_e-\gamma_e i}. \tag{B1}$$

We assume a Gaussian electric field profile,

$$E_j(t) = e^{-t^2\sigma_j^2/2}(e^{i\omega_j t}+e^{-i\omega_j t}), \tag{B2}$$

whose Fourier transform is a sum of two Gaussians (μ mean; σ std. dev.),

$$G(\omega;\mu,\sigma) = \frac{1}{\sigma\sqrt{2\pi}}e^{-(\omega-\mu)^2/2\sigma^2}, \tag{B3}$$

centered on the positive and negative central frequencies of the pulse,

$$\begin{aligned} E_j(\omega) &= \frac{1}{\sqrt{2\pi}\cdot\sigma_j}[e^{-(\omega-\omega_j)^2/2\sigma_j^2}+e^{-(\omega+\omega_j)^2/2\sigma_j^2}] \\ &= G(\omega;\omega_j,\sigma_j)+G(\omega;-\omega_j,\sigma_j). \end{aligned} \tag{B4}$$

Since the product of two Gaussian functions is itself a Gaussian function multiplied by a scaling factor,

$$\begin{aligned} &G(\omega;\mu_1,\sigma_1)G(\omega;\mu_2,\sigma_2) \\ &= \frac{1}{\sqrt{2\pi}}\frac{1}{\sqrt{\sigma_1^2\sigma_2^2}}\exp\left[\frac{-(\mu_1-\mu_2)^2}{2(\sigma_1^2+\sigma_2^2)}\right] \\ &\quad\times G\left(\omega;\frac{\mu_1\sigma_2^2+\mu_2\sigma_1^2}{\sigma_1^2+\sigma_2^2},\frac{\sigma_1\sigma_2}{\sqrt{\sigma_1^2+\sigma_2^2}}\right). \end{aligned} \tag{B5}$$

The integral in Eq. (B1) can be broken down into a sum over integrals of the following form:

$$\int_{-\infty}^{\infty}{\rm d}\,\omega\frac{G(\omega;\mu,\sigma)}{\omega-z} = \frac{-1}{\sigma}\sqrt{\frac{\pi}{2}}\Delta(z/\sigma\sqrt{2}), \tag{B6}$$

where $z\in\mathbb{C};{\rm Im}(z)>0$. These are calculated using the program MATHEMATICA. The lineshape function $\Delta(z)$ is

$$\Delta(z) = e^{-z^2}\left(\frac{{\rm Erf}(iz)}{i}-i\right). \tag{B7}$$

Expanding the electric field product from Eq. (B1) in terms of Gaussian functions

$$\begin{aligned} E^*_j(\omega)E_j(\omega-\omega_{fg}) &= G(\omega;\omega_j,\sigma_j)G(\omega;\omega_j+\omega_{fg},\sigma_j)+G(\omega;-\omega_j,\sigma_j)G(\omega;\omega_j+\omega_{fg},\sigma_j) \\ &\quad + G(\omega;\omega_j,\sigma_j)G(\omega;\omega_{fg}-\omega_j,\sigma_j)+G(\omega;-\omega_j,\sigma_j)G(\omega;\omega_{fg}-\omega_j,\sigma_j), \end{aligned} \tag{B8}$$

and using the Gaussian product expansion in Eq. (B5)

$$\begin{aligned} E^*_j(\omega)E_j(\omega-\omega_{fg}) &= \frac{1}{\sigma_j\sqrt{2\pi}}\times\left\{\exp\left[\frac{-\omega_{fg}^2}{4\sigma_j^2}\right]G\left(\omega;\omega_j+\frac{\omega_{fg}}{2},\frac{\sigma_j}{\sqrt{2}}\right)+\exp\left[\frac{-(2\omega_j+\omega_{fg})^2}{4\sigma_j^2}\right]G\left(\omega;\frac{\omega_{fg}}{2},\frac{\sigma_j}{\sqrt{2}}\right)\right. \\ &\quad\left.+\exp\left[\frac{-(2\omega_j-\omega_{fg})^2}{4\sigma_j^2}\right]G\left(\omega;\frac{\omega_{fg}}{2},\frac{\sigma_j}{\sqrt{2}}\right)+\exp\left[\frac{-\omega_{fg}^2}{4\sigma_j^2}\right]G\left(\omega;\frac{\omega_{fg}}{2}-\omega_j,\frac{\sigma_j}{\sqrt{2}}\right)\right\}, \end{aligned} \tag{B9}$$

the integral given in Eq. (B6) can be applied to each term in Eq. (B9)

$$\int_{-\infty}^{\infty}\frac{\mathrm{d}\,\omega}{2\pi}\frac{E_j^*(\omega)E_j(\omega-\omega_{fg})}{\omega-\omega_{fg}-\omega_e-\gamma_e i}=\left(\frac{-1}{\sigma_j^2\sqrt{2}}\right)\times\left\{\exp\left[\frac{-\omega_{fg}^2}{4\sigma_j^2}\right]\Delta\left[\left(\omega_e+\frac{\omega_{fg}}{2}-\omega_j+i\gamma_e\right)\Big/\sigma_j\right]\right.$$
$$+\exp\left[\frac{-(2\omega_j+\omega_{fg})^2}{4\sigma_j^2}\right]\cdot\Delta\left[\left(\omega_e+\frac{\omega_{fg}}{2}-\omega_j+i\gamma_e\right)\Big/\sigma_j\right]$$
$$+\exp\left[\frac{-(2\omega_j-\omega_{fg})^2}{4\sigma_j^2}\right]\cdot\Delta\left[\left(\omega_e+\frac{\omega_{fg}}{2}-\omega_j+i\gamma_e\right)\Big/\sigma_j\right]$$
$$\left.+\exp\left[\frac{-\omega_{fg}^2}{4\sigma_j^2}\right]\cdot\Delta\left[\left(\omega_e+\frac{\omega_{fg}}{2}-\omega_j+i\gamma_e\right)\Big/\sigma_j\right]\right\}. \tag{B10}$$

The second and third terms in Eq. (B10) will be negligibly small if $\omega_j(\sim 2473\mathrm{eV})\gg 1/\sigma_j(10\,\mathrm{eV})$, leaving

$$\int_{-\infty}^{\infty}\frac{\mathrm{d}\,\omega}{2\pi}\frac{E_j^*(\omega)E_j(\omega-\omega_{fg})}{\omega-\omega_{fg}-\omega_e-i\gamma_e}=\mathcal{I}_j\left[\omega_{fg},\omega_e+\frac{\omega_{fg}}{2}+i\gamma_e\right] \tag{B11}$$

with the function

$$\mathcal{I}_j\left[\omega_{fg},\omega_e+\frac{\omega_{fg}}{2}+i\gamma_e\right]=\frac{-\sqrt{2}}{\sigma_j^2}\times\exp\left[\frac{-\omega_{fg}^2}{4\sigma_j^2}\right]\cdot\Delta\left[\left(\omega_e+\frac{\omega_{fg}}{2}-\omega_j+i\gamma_e\right)\Big/\sigma_j\right].$$

Equation (B12) is the analytic form of the electric field weighting function described in Ref. 12 for Gaussian pulses.

The final result is that for an x-ray experiment, the weighting of the transition is given by the product of a Gaussian and a lineshape function $\Delta(z)$. The real and imaginary parts of $\Delta(z)$ are plotted in Fig. 10. For excited states with a lifetime one tenth of the spectral bandwidth of the pulse, the function $1/(z+i)$ is a good approximation to $\Delta(z)$ (see Fig. 10, bottom). Inserting this approximation into Eq. (B12)

$$\sum_e \mu_{fe}\mu_{eg}\mathcal{I}_j\left[\omega_{fg},\omega_e+\frac{\omega_{fg}}{2}+i\gamma_e\right]\sim\sum_e\frac{\mu_{fe}\mu_{eg}\dfrac{\sqrt{2}}{\sigma_j}\exp\left[\dfrac{-\omega_{fg}^2}{4\sigma_j^2}\right]}{\omega_j-\omega_e-\dfrac{\omega_{fg}}{2}-(\gamma_e+\sigma_j)i},$$

a Kramers–Heisenberg expression with each dipole moment multiplied by a factor representing the spectral strength of the pulse at the average energy absorbed in both interactions with the field,

$$\mu_{fe,eg}\to\mu_{fe,eg}\exp\left[\frac{-(\omega_{fg}/2)^2}{2\sigma_j^2}\right] \tag{B12}$$

and the lifetime of the excited state including the spectral bandwidth of the pulse

$$\gamma_e\to\gamma_e+\sigma_j. \tag{B13}$$

We will denote this approximation, which is useful when the detuning is small compared to the core-hole width the mutually independent decay approximation. The uncertainty in the excited state lifetime has a contribution from the core-hole lifetime ($\tau_e\sim 1/\gamma_e$), and the temporal width of the pulse ($\tau_j\sim 1/\sigma_j$), if the lifetimes due to these two processes are treated as mutually independent exponential distributions, their joint probability is the product

$$e^{-\tau/\tau_e}e^{-\tau/\tau_j}\propto e^{\tau/[(\tau_e\tau_j)/(\tau_e+\sigma_j)]} \tag{B14}$$

which is equivalent to the modification of the excited state lifetime given in Eq. (B13).

APPENDIX C: THE HARTREE–FOCK STATIC-EXCHANGE APPROXIMATION FOR THE CORE-EXCITED STATES

Previously, we have simulated the nonlinear x-ray spectra by calculating the many-electron states of the equivalent-core molecules with N, $N+1$, and $N+2$ electrons in the presence of zero, one, and two core-holes, respectively, at the ECA level.[12] The valence and core-excited states were approximated as singly and doubly substituted Slater determinants with Hartree–Fock orbitals (or Kohn–Sham orbitals in density functional theory). The core transitions were described by the valence transitions of the equivalent-core molecules, where the effect of the created core-hole on the valence electrons is reduced to that of a static Coulomb potential of a positive charge, i.e., the nuclear number is increased by 1. The lowest core-excited state was described by the ground state of the $N+1$ valence electrons (the additional electron accounts for the promoted core electron) in the field of the core-hole. The high-lying core-excited state manifold is then described by the excitations among the $N+1$ electrons within the valence orbital space.

According to Koopmans' theorem,[49] the first ionization energy of a molecule is given to a good approximation by the negative of the orbital energy of the highest occupied molecular orbital. This relation is exact when all orbitals are frozen, i.e., do not change upon electronic excitation and provides a qualitatively correct description for low-lying excited states (even though electron correlation effects are neglected). For high-lying excited states such as those involving core electronic excitations, an improved description of orbital relaxation effects is crucial. The ECA uses the weak electron correlation due to the large separation in energy between the core orbital space and valence orbital space, and represents the core-hole simply as a positive charge. This can only be used for K-edge electronic excitations where a deep core (i.e., $1s$) electron is promoted.

STEX is a higher-level single-particle approximation, which offers an improved description of orbital relaxation, not limited to deep core electronic excitations, and allows to study various core-hole configurations including shallow holes. STEX is justified by the large energy separation between the core and valence orbital spaces. The deeper core orbitals are usually well localized, and correlations involving such orbitals are weak. Electron correlation effects become increasingly important for shallower holes.

Below we briefly summarize the HF–STEX approximation, and outline the procedure used for calculating the core-excited states, as well as the transition frequencies and transition dipole moments between valence-excited states with no core-hole and core-excited states with one localized core-hole. STEX involves the following steps:[20]

- Compute the ground state orbitals of the neutral molecule at the HF level.
- Use ΔSCF (Refs. 46 and 50) to generate the relaxed orbitals of the ion where a selected core electron is removed from the neutral molecule.
- Construct the STEX Hamiltonian based on the relaxed orbitals obtained from the ΔSCF calculation and transform it by projecting out the occupied orbitals of the target ionic state obtained from the ΔSCF calculation.
- Generate the virtual orbitals of the core-excited state by diagonalizing the projected STEX Hamiltonian.

The core-excited state for molecules with a closed-shell ground state is constructed using the occupied orbitals of target ionic state obtained from the ΔSCF calculation and the virtual orbitals obtained by diagonalizing the projected STEX Hamiltonian,

$$\left|\Psi_{j,\epsilon}^{N}\right\rangle = \frac{1}{\sqrt{2}}\left(a_{\epsilon_\alpha}^{\dagger}\left|\Psi_{j_\alpha}^{N-1}\right\rangle + a_{\epsilon_\beta}^{\dagger}\left|\Psi_{j_\beta}^{N-1}\right\rangle\right) \tag{C1a}$$

with

$$\left|\Psi_{j_\alpha}^{N-1}\right\rangle = a_{j_\alpha}\left|\Psi_{\mathrm{ref}}^{N}\right\rangle, \quad \left|\Psi_{j_\beta}^{N-1}\right\rangle = a_{j_\beta}\left|\Psi_{\mathrm{ref}}^{N}\right\rangle, \tag{C1b}$$

where the reference state $|\Psi_{\mathrm{ref}}^{N}\rangle$ is the closed-shell Hartree–Fock ground state of the neutral molecule and $|\Psi_{j}^{N-1}\rangle$ is the target ionic state with an electron removed from core orbital φ_j. $a_{j_\alpha}(a_{j_\beta})$ annihilates an alpha (beta) electron in core orbital φ_j and $a_{\epsilon_\alpha}^{\dagger}(a_{\epsilon_\beta}^{\dagger})$ creates an alpha (beta) electron in virtual orbital φ_ϵ.

The total core-excited state energy expressed in the molecular orbital basis is

$$E = \sum_{i\neq j,\epsilon}^{occ}\left(h_{ii} + F_{ii}^{\Delta\mathrm{SCF}}\right) + F_{jj}^{\Delta\mathrm{SCF}} + F_{\epsilon\epsilon}^{\Delta\mathrm{SCF}} + \langle jj|\epsilon\epsilon\rangle + \langle j\epsilon|\epsilon j\rangle, \tag{C2}$$

where $F^{\Delta\mathrm{SCF}}$ is the Fock operator of the target ionic state for the ΔSCF calculation.

$$F^{\Delta\mathrm{SCF}} = h + \sum_{i\neq j,\epsilon}^{occ}(2J_i - K_i), \tag{C3}$$

where h is the one-electron operator, describing the kinetic energy and nuclear attraction of an electron. J_i and K_i are the closed-shell Coulomb and exchange operators. For a chosen electron 1, the one-electron operator is

$$h(1) = -\frac{1}{2}\nabla_1^2 - \sum_A \frac{Z_A}{r_{1A}}, \tag{C4}$$

the Coulomb operator is

$$J_i(1) = \int d\mathbf{r_2}\psi_i^*(2)\, r_{12}^{-1}\psi_i(2), \tag{C5}$$

and the exchange operator is

$$K_i(1)\,\psi_a(1) = \left[\int d\mathbf{r_2}\psi_i^*(2)\, r_{12}^{-1}\psi_a(2)\right]\psi_i(1). \tag{C6}$$

The virtual orbital φ_ϵ is calculated variationally by the functional derivative of the energy with respect to this orbital, which then gives rise to the corresponding Fock operator, known as the static-exchange Hamiltonian,

$$F^{\mathrm{STEX}} = h + \sum_{i\neq j,\epsilon}^{\mathrm{occ}}(2J_i - K_i) + J_j + K_j. \tag{C7}$$

The eigenvalues ε_ϵ of Eq. (C7) are solved by projecting the static-exchange Hamiltonian on a basis set orthogonalized to the occupied orbitals of the target ionic state obtained from the ΔSCF calculation. The transition frequencies are then given by $E_{j,\epsilon}^{N} = E_j^{N-1} + \varepsilon_\epsilon - E_0^N = IP_j + \varepsilon_\epsilon$, where E_j^{N-1} is the energy of the target ionic state upon electron ionization from the jth molecular orbital, E_0^N is energy of the neutral molecule, and $IP_j = E_j^{N-1} - E_0^N$ is the ionization potential upon electron ionization from the jth molecular orbital.

The transition dipole moments are given by $\mu_{fg'} = \langle f|\hat{\mu}(\boldsymbol{r})|g'\rangle$, where g' and f are the valence-excited states with all core orbitals doubly occupied, and the core-excited states of the molecule with a core-hole, respectively. $\hat{\mu}(\boldsymbol{r})$ is the dipole operator. Two sets of orbitals are separately optimized for each state. The orbitals are orthogonal within each set, but the two sets of orbitals are nonorthogonal to each other. To calculate the transition dipole moments between the two states, we must compute the cofactors (electronic Franck–Condon overlaps) as described in Ref. 51.

In summary, both ECA and STEX generate relaxed orbitals for core electronic excitations. STEX uses ΔSCF to

obtain the relaxed orbitals for the corresponding ion by removing the core electron from the neutral molecule. The ECA uses a different nuclear charge (i.e., increase the nuclear number by 1) for the atom where the core-hole is localized, and consequently requires to add one electron to the valence orbital space. An obvious limitation of the ECA is the inherently incorrect spin symmetry. Efforts had been made to overcome this problem in the conventional equivalent-core approximation.[14] Another drawback is its inability to describe shallow core electronic excitations, for which the effects of core-hole cannot be simply replaced by a static Coulomb potential. STEX overcomes these limitations and can be easily implemented to shallow holes by keeping track of which orbital the electron is removed from the neutral molecule, providing a straightforward way to study hole-migration effects for shallow holes.[52–56]

APPENDIX D: ECA VERSUS STEX

We define a coordinate frame with the origin on the resonant core-atom. ($\mathbf{R}_n \equiv 0$) Vectors $\mathbf{r}$ and $\mathbf{r}'$ have lengths r and r', respectively. In the STEX approximation, the valence-core interaction is written as an effective one-particle field,

$$v_c(\mathbf{r}) = -\int \frac{|\phi_c(\mathbf{r}')|^2}{|\mathbf{r}-\mathbf{r}'|}\mathrm{d}\,\mathbf{r}'. \tag{D1}$$

Inserting a radially symmetric exponentially decaying function for the tightly bound 1*s* orbital,

$$\phi_c(\mathbf{r}) = \sqrt{\frac{\alpha^3}{\pi}}e^{-\alpha r} \tag{D2}$$

we get the following expression for the potential:

$$v_c(\mathbf{r}) = \frac{e^{-2\alpha r}\left(\frac{1+\alpha r}{r}\right)-1}{r}. \tag{D3}$$

This potential can be divided into two terms. $v_{\mathrm{ECA}}(\mathbf{r}) = -1/r$ is the field generated by a point charge centered on the atom. The effect of the core-potential will depend on the shape of the valence orbitals and is included in the term $v_\Delta(\mathbf{r}) = e^{-2\alpha r}(1-\alpha r)/r$ (see Fig. 11). The spatial extent of the core-orbital reduces the potential near the core

$$\lim_{r\to 0^+} v_c(\mathbf{r}) = -\alpha \quad \neq \quad \lim_{r\to 0^+} v_{\mathrm{ECA}}(\mathbf{r}) = -\infty. \tag{D4}$$

The valence orbitals will be renormalized with respect to this "softened" potential $v_c(\mathbf{r})$. Non-ECA terms will be large when the matrix element

$$\langle\phi_p|v_\Delta(\mathbf{r})|\phi_q\rangle = \int \phi_p^*(\mathbf{r})\frac{e^{-2\alpha r}(1-\alpha r)}{r}\phi_q(\mathbf{r})\mathrm{d}\,\mathbf{r} \tag{D5}$$

is large. Expanding $\phi_{p,q}(\mathbf{r})$ in a Taylor series around $\mathbf{r} = \mathbf{R}_n = 0$

$$\begin{aligned}\phi_p^*(\mathbf{r}) &= \phi_p^*(0) + \mathbf{r}\cdot\nabla\phi_p^*(0) + \mathcal{O}^{(2)},\\ \phi_q(\mathbf{r}) &= \phi_q(0) + \mathbf{r}\cdot\nabla\phi_q(0) + \mathcal{O}^{(2)}.\end{aligned} \tag{D6}$$

and inserting into Eq. (D5), we get

$$\langle\phi_p|v_\Delta(\mathbf{r})|\phi_q\rangle = \frac{2\pi}{\alpha^3}\phi_p^*(0)\phi_q(0) + \frac{3\pi}{2\alpha^4}\nabla\phi_p^*(0)\nabla\phi_q(0). \tag{D7}$$

If we treat the core-hole perturbation on the valence electrons as a rank-one perturbation, and neglect off-diagonal matrix elements in Eq. (D7), we see that the non-ECA contribution to the valence orbital energy shifts will be greatest for orbitals with a high amplitude or gradient in the neighborhood of the core-hole.

[1] M. M. Murnane, H. C. Kapteyn, M. D. Rosen, and R. W. Falcone, Science **251**, 531 (1991).
[2] R. W. Schoenlein, S.Chattopadhyay, H. H. W. Chong, T. E. Glover, P. A. Heimann, C. V. Shank, A. A. Zholents, and M. S. Zolotorev, Science **287**, 2237 (2000).
[3] M. Drescher, M. Hentschel, R. Keinberger, G. Tempea, C. Spielmann, G. A. Reider, P. B. Corkum, and F. Krausz, Science **291**, 1923 (2001).
[4] C. Bressler and M. Chergui, Chem. Rev. **104**, 1781 (2004).
[5] M. Chergui and S. Mukamel, Chem. Phys. **299**, 155 (2004).
[6] S. Mukamel, Phys. Rev. B **72**, 235110 (2005).
[7] P. H. Bucksbaum, Science **317**, 766 (2007).
[8] M. F. Kling and M. J. J. Vrakking, Ann. Rev. Phys. Chem. **59**, 463 (2008).
[9] F. Krausz and M. Ivanov, Rev. Mod. Phys. **81**, 163 (2009).
[10] R. Santra, N. V. Kryzhevoi, and L. S. Cederbaum, Phys. Rev. Lett. **103**, 013002 (2009).
[11] S. Tanaka and S. Mukamel, Phys. Rev. Lett. **89**, 043001 (2002).
[12] I. Schweigert and S. Mukamel, Phys. Rev. A **76**, 012504 (2007).
[13] W. H. E. Schwarz and R. Buenker, Chem. Phys. **13**, 153 (1976).
[14] M. Wohlfarth and L. S. Cederbaum, J. Chem. Phys. **116**, 8723 (2002).
[15] T. W. Whitfield, G. J. Martyna, S. Allison, S. P. Bates, and J. Crain, Chem. Phys. Lett. **414**(1–3), 210 (2005).
[16] T. Hayashi, W. Zhuang, and S. Mukamel, J. Phys. Chem. A **109**(43), 9747 (2005).
[17] T. Hayashi and S. Mukamel, J. Chem. Phys. **125**(19), 194510 (2006).
[18] H. Ågren, V. Carravetta, O. Vahtras, and L. G. M. Pettersson, Chem. Phys. Lett. **222**, 75 (1994).
[19] H. Ågren, V. Carravetta, and L. G. M. Pettersson, Phys. Rev. B **53**, 16074 (1996).
[20] H. Ågren, V. Carravetta, O. Vahtras, and L. G. M. Pettersson, Theor. Chem. Acc. **97**, 14 (1997).
[21] V. Carravetta, O. Plashkevych, and H. Ågren, Chem. Phys. **263**, 231 (2001).
[22] W. Hunt and W. Goddard, Chem. Phys. Lett. **3**, 414 (1969).
[23] I. Schweigert and S. Mukamel, Phys. Rev. A **78**, 052509 (2008).
[24] L. Young, E. P. Kanter, B. Krssig, Y. Li, A. M. March, S. T. Pratt, R. Santra, S. H. Southworth, N. Rohringer, L. F. DiMauro, G. Doumy, C. A. Roedig, N. Berrah, L. Fang, M. Hoener, P. H. Bucksbaum, J. P. Cryan, S. Ghimire, J. M. Glownia, D. A. Reis, J. D. Bozek, C. Bostedt, and M. Messerschmidt, Nature (London) **466**(7302), 56 (2010).
[25] M. Hoener, L. Fang, O. Kornilov, O. Gessner, S. T. Pratt, M. Ghr, E. P. Kanter, C. Blaga, C. Bostedt, J. D. Bozek, P. H. Bucksbaum, C. Buth, M. Chen, R. Coffee, J. Cryan, L. DiMauro, M. Glownia, E. Hosler, E. Kukk, S. R. Leone, B. McFarland, M. Messerschmidt, B. Murphy, V. Petrovic, D. Rolles, and N. Berrah, Phys. Rev. Lett. **104**(25), 253002 (2010).
[26] A. I. Kuleff, J. Breidbach, and L. S. Cederbaum, J. Chem. Phys. **123**(4), 044111 (2005).
[27] A. Cesar, F. Gel'mukhanov, Y. Luo, H. Ågren, P. Skytt, P. Glans, J. Guo, K. Gunnelin, and J. Nordgren, J. Chem. Phys. **106**, 3439 (1996).
[28] Y. Velkov, V. Kimberg, N. Kosugi, P. Salek, and F. Gel'mukhanov, Chem. Phys. Lett. **476**, 147 (2009).
[29] U. Harbola and S. Mukamel, Phys. Rev. B **79**, 085108 (2009).
[30] S. Rahav and S. Mukamel, Adv. At., Mol., Opt. Phys. **59**, 223 (2010).
[31] S. Mukamel, *Principles of Nonlinear Optical Spectroscopy* (Oxford University Press, New York, 1995).
[32] Y. Yan and S. Mukamel, Phys. Rev. A **41**, 6485 (1990).
[33] R. Martin, J. Chem. Phys. **118**, 4775 (2003).
[34] J. Itatani, J. Levesque, D. Zeidler, H. Niikura, H. Pépin, J. C. Kieffer, P. B. Corku, and D. M. Villeneuv, Nature (London) **432**, 867 (2004).
[35] W. Li, X. Zhou, R. Lock, S. Patchkovskii, A. Stolow, H. C. Kapteyn, and M. M. Murnane, Science **322**, 1207 (2008).
[36] O. Smirnova, Y. Mairesse, S. Patchkovskii, N. Dudovich, D. Villeneuve, P. Corkum, and M. Y. Ivanov, Nature (London) **460**, 972 (2009).
[37] S. Mukamel and H. Wang, Phys. Rev. A **81**(6), 062334 (2010).
[38] M. J. Frisch, G. W. Trucks, H. B. Schlegel *et al.*, GAUSSIAN03, Revision B.05, Gaussian, Inc., Wallingford, CT, 2004.

[39]T. D. Crawford, C. D. Sherrill, E. Valeev, J. Fermann, R. King, M. Leininger, S. Brown, C. Janssen, E. Seidl, J. Kenny, and W. Allen, J. Comput. Chem. **28**, 1610 (2007).
[40]C. P. Schwartz, R. J. Saykally, and D. Prendergast, J. Chem. Phys. **133**(4), 044507 (2010).
[41]J. A. Bearden and A. F. Burr, Rev. Mod. Phys. **39**(1), 125 (1967).
[42]S. T. Perkins, D. E. Cullen, M. H. Chen, J. H. Hubbell, J. A. Rathkopf, and J. H. Scofield, Lawrence Livermore National Laboratory Report UCRL-50400, Vol. 30, Livermore, Calif, 1991.
[43]J. H. Hubbell, P. N. Trehan, N. Singh, B. Chand, D. Mehta, M. L. Garg, R. R. Garg, S. Singh, and S. Puri, A Review, Bibliography, and Tabulation of K, L, and Higher Atomic Shell X-Ray Fluorescence Yields, J. Phys. Chem. Ref. Data **23**(2), 339 (1994).
[44]M. Rohlfing and S. G. Louie, Phys. Rev. Lett. **81**(11), 2312 (1998).
[45]A. B. Trofimov, I. L. Krivdina, J. Weller, and J. Schirmer, Chem. Phys. **329**(1–3), 1 (2006).
[46]T. Helgaker, P. Jørgensen, and J. Olsen, *Molecular Electronic-Structure Theory* (Wiley, New York, 2000).
[47]E. Davidson, *Reduced Density Matrices in Quantum Chemistry* (Academic, New York, 1976).
[48]L. N. Trefethen and D. Bau III, *Numerical Linear Algebra* (SIAM, Philadelphia, 1997), Part I, Lecture 4, pp. 25–30.
[49]A. Szabo and N. Ostlund, *Modern Quantum Chemsitry* (Dover, New York, 1996).
[50]M. Guest and V. Saunders, Mol. Phys. **28**, 819 (1974).
[51]D. Cook, *Handbook of Computational Quantum Chemistry* (Dover, New York, 2005).
[52]R. Weinkauf, P. Schanen, D. Yang, S. Soukara, and E. W. Schlag, J. Phys. Chem. **99**, 11255 (1995).
[53]R. Weinkauf, P. Schanen, A. Metsala, E. W. Schlag, M. Bürgle, and H. Kessler, J. Phys. Chem. **100**, 18567 (1996).
[54]J. Breibach and L. S. Cederbaum, J. Chem. Phys. **118**, 3983 (2003).
[55]J. Breibach and L. S. Cederbaum, J. Chem. Phys. **126**, 034101 (2007).
[56]F. Remacle and R. D. Levine, Proc. Natl. Acad. Sci. U.S.A. **103**, 6793 (2006).